ROYAL SOCIETY
OF CHEMISTRY

Environmental Science: Nano

ARTICLE

Highly efficient and selective extraction of uranium from aqueous solution by a magnetic device: succinyl-β-cyclodextrin-APTES@maghemite nanoparticles

A. S. Helal,[a,b,c*] E. Mazario,[a] A. Mayoral,[d] P. Decorse,[a] R. Losno,[e] C. Lion,[a] S. Ammar[a] and M. Hémadi [a*]

The removal of radio-elements, notably uranium, from waste-waters is crucial for public health and environmental remediation. To this end, succinyl-β-cyclodextrin (SβCD) is grafted onto maghemite nanoparticles (NPs) synthesized by the polyol method. The nanocomposite was well characterized. The adsorption of U(VI) by SβCD-APTES@Fe$_2$O$_3$ is pH-dependent with a maximum at pH 6. Adsorption occurs mainly by complex formation and displays a very good selectivity for U(VI) compared to other cations such as Cs$^+$, K$^+$, Na$^+$, Mg^{2+} and Al^{3+}. The data were plotted according to the Langmuir, Freundlich, Elovich, Temkin and Halsey isotherms. The Langmuir isotherm maximum adsorption capacity (q$_{max}$) is 286 mg U g^{-1} and higher than for other reported sorbents. Moreover, C$_s$-corrected STEM visualizes the uranium on the NP surface, which is consistent with the Halsey isotherm model for multilayer adsorption. The U(VI) adsorbed on SβCD-APTES@Fe$_2$O$_3$ is easily recovered by magnetic sedimentation and desorption performed in a small volume in order to concentrate the extract. The nanocomposite can be regenerated and re-used at least tenfold.

1. Introduction

Apart from being radioactive, uranium is highly toxic in all its oxidation states and causes severe damage to bones, kidney, neurological system, etc.[1-3] Nevertheless, it is used as a fuel in nuclear power plants and, to a lesser extent, in reactors for the propulsion of naval vessels, for basic and applied research, and for the production of radioisotopes for medical applications, such as cancer therapy and imaging.[4, 5] The contamination of soil and water by highly radio-toxic elements, not only by uranium, but also by cesium and plutonium, released accidentally during nuclear disasters or routine maintenance of power plants, can be the cause of severe health and ecological problems.[6, 7] For this reason radioactive pollution is of high social and environmental concern, and it is increasingly important to devise procedures for depollution.[1, 2]

To date, many physical and chemical methods have been investigated and/or used for the remediation of heavy-metal

contamination.[8] These include solvent extraction,[9-12] chemical precipitation,[13, 14] ion-exchange resins,[15-18] membrane-based extraction[19, 20] and electrochemical extraction.[21-23] However, these processes are time-consuming and present several drawbacks, such as excessive use of organic solvents, complex equipment, large secondary waste and prefiltration problems, which limit their efficiency. The aim is to overcome these disadvantages by the development of compact modular processes that provide an easy-to-handle separation technique.[24] Recently sorption has aroused interest as an alternative to conventional ion-exchange resins for the recovery of metal ions from low-concentration effluents.[25-29] It is now widely adopted in the field of environmental protection because it is a highly efficient, environment-friendly and inexpensive technique. A great number of new adsorbent materials have been synthesized for the solid/liquid separation of metal ions, such as membranes, modified fibers, carbon nanotubes, hydrogels, mesoporous silica and magnetic materials.[30, 31] Despite this considerable progress, prior functionalization of the surface of the sorbent by a specific chelating agent, such as polyamidoxime, metal ion-imprinted polymer materials, carboxylate or hydroxyl, is still required.[32]

Magnetic materials and especially iron oxide nanoparticles are being investigated for a wide range of applications, including targeted drug delivery,[33] hyperthermia,[34, 35] photothermia,[36, 37] bio-imaging,[38] catalysis,[39] and environmental remediation.[40] They have several advantages, the six most important of which are in our opinion: (1) easy collection and removal from a complex multiphase system by an external magnetic field, which makes solid-liquid phase separation fast and simple, as

a. ITODYS – Interfaces, Traitements, Organisation et Dynamique des Systèmes, Université Paris Diderot, Sorbonne Paris Cité, CNRS-UMR 7086, Paris, France
b. Department of Nuclear Science and Engineering, Massachusetts Institute of Technology, USA.
c. Nuclear Materials Authority, P.O Box 540 El Maadi, Cairo, Egypt.
d. Laboratorio de Microscopias Avanzadas (LMA), Instituto de Nanociencia de Aragón (INA) - Universidad de Zaragoza, Spain
e. Institut de Physique du Globe de Paris, Sorbonne Paris Cité, UMR 7154, CNRS, F-75005 Paris, France.
* Emails: hemadi@univ-paris-diderot.fr or ashelal@mit.edu

ARTICLE

well as highly effective;[41] (2) low-cost and low reagent consumption; (3) high selectivity and easy automation; (4) high pre-concentration factors and eco-friendliness; (5) reusable adsorbent; (6) combination with modern detection techniques in on-line or off-line mode.[24]

However, their main disadvantage lies in the strong dipole-dipole attraction between particles and their tendency to aggregate, which reduces their adsorption capabilities.[42] To overcome this problem, specifically designed heavy-metal chelating groups are interesting candidates for functionalizing the surfaces of the magnetic nanoparticles (MNPs). β-Cyclodextrin (β-CD) is a cyclic oligosaccharide consisting of seven α-D-glucose units connected through α-(1,4) bonds. These molecules are toroidal, truncated cones containing a cavity with primary and secondary hydroxyl groups at the smaller and larger openings, respectively.[43-45] Cyclodextrins form inclusion complexes with a wide variety of organic and inorganic compounds in the relatively hydrophobic cavity.[44] Some chemical properties, such as aqueous solubility and metal complexation potentials, can be altered by introducing functional groups on the outside of the cyclodextrin.[46] This work aims at preparing a highly efficient functionalized magnetic nanocomposite adsorbent with high adsorption capacity (Scheme 1).
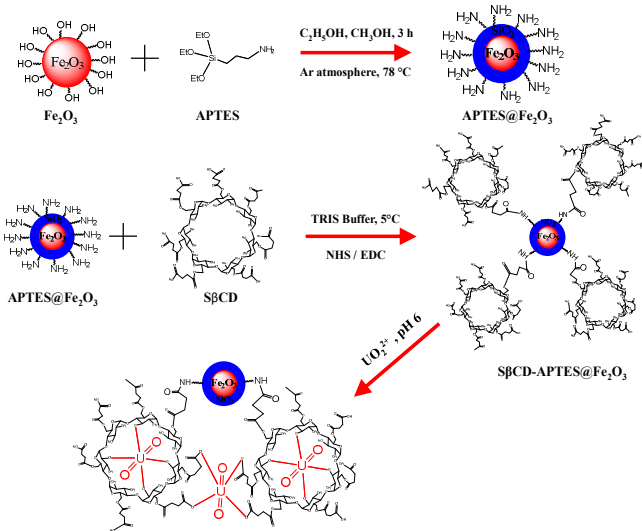
Scheme 1: Synthesis, functionalization of nanoparticles (APTES@Fe$_2$O$_3$) and uranium(VI) extraction strategy using SβCD-APTES@Fe$_2$O$_3$.

To this end, an original nanodevice, an SβCD-APTES@Fe$_2$O$_3$ nanocomposite, is synthesized by grafting succinyl-β-cyclodextrin (SβCD) onto APTES@Fe$_2$O$_3$. Indeed, a prior functionalization of Fe$_2$O$_3$ by APTES covers its surface with amino functions which are used to attach SβCD to the nanoparticles via the formation of covalent amide bonds with the carboxylic groups. The resulting nanocomposite is characterized by a variety of techniques: Spherical-aberration-corrected (C$_s$-corrected) STEM, FTIR, XRD, XPS, TGA, and VSM analysis. Nano-Isothermal Titration Calorimetry (nano-ITC) is used to investigate the coordination of uranium. The influence

of various experimental parameters on adsorption, such as pH, contact time and the initial U(VI) concentration are studied. Selectivity, adsorption isotherms and kinetic models of the sorption process are also investigated.

2. Results and discussion

2.1 Characterization

2.1.1 Nanocomposite. The XRD spectra of Fe$_2$O$_3$ and SβCD-APTES@Fe$_2$O$_3$ nanoparticles are shown in Figure S1. No extra peaks related to foreign crystalline contamination, such as hematite (α-Fe$_2$O$_3$), iron hydroxides (Fe(OH)$_3$, FeOH) or iron oxyhydroxides (FeOOH) are observed. The nanocrystallite size, calculated by Rietveld analyses is 8.4 ± 0.5 nm. The agreement factors are R$_{bragg}$ = 1.727 and R$_{f-factor}$ = 1.398. Surface functionalization causes some reduction in the peak intensity and a small increment in the background at low angle compared to the original pattern of uncoated MNPs. Transmission electron microscopy (TEM) images of APTES@Fe$_2$O$_3$ and SβCD-APTES@Fe$_2$O$_3$ (Figure S2 a-d) are given for a few particles in order to show clearly the successive increases in thickness due to the coating of the MNPs by different organic materials. These images indicate that the MNP surface is functionalized. This is confirmed by thermogravimetric analysis (TGA) of SβCD-APTES@Fe$_2$O$_3$ NPs. The total weight loss is about 14 % (Figure S3), and appears as a small heat absorption at 261 °C due to the decomposition of the organic coating (SβCD-APTES).

2.2 Uranyl-Nanocomposite. Before the adsorption of uranyl, the FTIR spectrum of the SβCD-APTES@Fe$_2$O$_3$ nanocomposite shows three characteristic peaks at 691, 1634 and 3407 cm^{-1}, which are attributed to Si–O stretching, the C=O in the amide bond (H–N-C=O), and O-H bending vibrations, respectively (Figure S4).[47, 48] The peaks at 1077 and 1158 cm^{-1} are attributed to the glycosidic C-O-C or C-C/C-O stretching vibrations.[49, 50] The peak at 1727 cm^{-1} is assigned to the C=O stretching vibration,[43] which confirms the presence of SβCD in the adsorbent. After U(VI) adsorption a new characteristic sharp peak of UO$_2^{2+}$ is observed at 923 cm^{-1}.[12, 51-55] Furthermore, the absorption frequency shifts from 1727 cm^{-1} to 1733 cm^{-1} due to coordination of carbonyl groups with UO$_2^{2+}$. Other shifts confirm complex formation between UO$_2^{2+}$ and the succinyl moiety: shifts of 23 cm^{-1} for the asymmetric carboxylic stretching from 1407 and 1563 cm^{-1} to 1384 and 1540 cm^{-1}, respectively.[49] The peaks at 1030, 1158, and 3407 cm^{-1}, corresponding to the antisymmetric glycosidic C-O-C vibrations, coupled (C-C/C-O) and OH stretching vibrations, respectively, shift to 1028, 1157, and 3392 cm^{-1}, respectively, indicating that the oxygen atom is directly involved in interaction with UO$_2^{2+}$.[43] Therefore, uranium interacts and forms complexes with SβCD-APTES@Fe$_2$O$_3$ by coordination.

The XPS survey spectra of SβCD-APTES@Fe$_2$O$_3$ before and after U(VI) sorption are displayed in Figures 1a1 and 1a2. Before sorption, the characteristic peaks of SβCD-APTES@Fe$_2$O$_3$ are Fe2p

(doublet), O1s, C1s and N1s centered at 711.1-723.5 eV (which is in agreement with the presence of Fe_2O_3), 532 eV, 286 eV and 399.3 eV, respectively. The high-resolution spectra display a three-component C1s peak (Figure 1e1): the first includes C-C and C-H components at 285 eV related to atmospheric contamination of the sample, a large component at 286.4 eV for C-OH and a weak one at 289 eV for O=C-O. The N1s peak consists of two components (Figure 1d1): the first at 399.3 eV (H-N-C=O) is due to the amide bond between SβCD and the APTES grafted onto Fe_2O_3, and the second at 402.1 eV is that of the residual amino function of APTES, NH^+. The O1s peak (Figure 1f1) also consists of two components: the first is that of the oxygens of Fe_2O_3 (530 eV) while the second is that of the organic oxygens of SβCD-APTES (≈532.5-533 eV). Uranium is not detected in this sample.
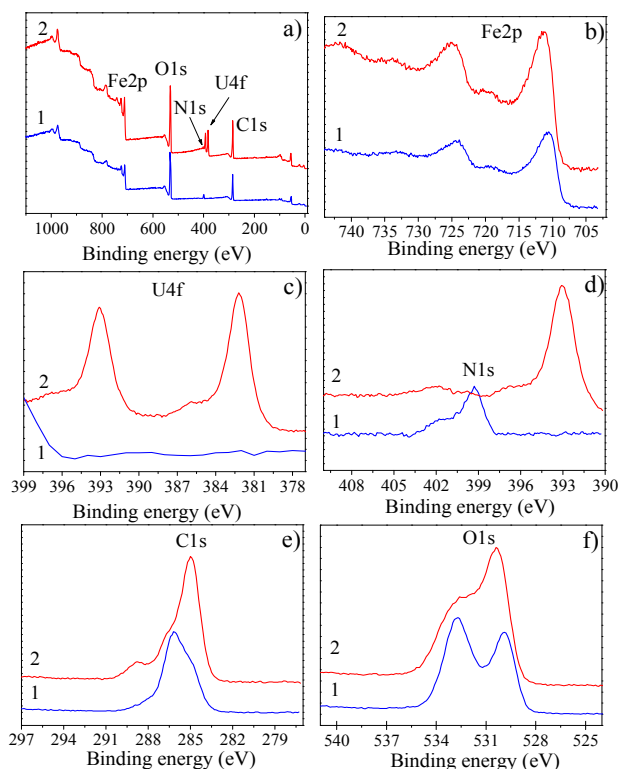

Figure 1. XPS spectra of SβCD-APTES@Fe_2O_3 NPs; lines (1) before U(VI) adsorption, lines (2) after U(VI) adsorption: (a) Survey spectra, (b) High-resolution Fe2p ($2p_{1/2}$ and $2p_{3/2}$) spectra, (c) High-resolution U4f ($4f_{5/2}$ and $4f_{7/2}$) spectra from U-loaded SβCD-APTES@Fe_2O_3. (d), (e) and (f) High-resolution spectra for N1s, C1s and O1s, respectively.

After sorption, an additional peak (doublet) appears at 382.2 and 393.1 eV (Figure 1a2, 1c2), corresponding to the 4f photoelectron peaks of U(VI), $U4f_{7/2}$ and $U4f_{5/2}$, respectively, complexed with the succinyl carboxylate groups. The binding energies are in good agreement with the literature.[56] The high-resolution spectra show a small variation in the N1s peak whereas the component at 399.3 eV disappears and the intensity at 402.5 eV decreases because the nitrogen is partially hidden by the uranium. Furthermore, an increase in the intensity of the component at 289 eV occurs because of the carbon of the uranium acetate. These results further

confirm that uranyl ions are adsorbed on the surface of SβCD-APTES@Fe_2O_3, and are in good agreement with FTIR.

The structures of the SβCD-APTES@Fe_2O_3 NPs as well as the location of U(VI) at their surface were visualized by spherical-aberration-corrected STEM. When C_s-corrected STEM is combined with a HAADF detector, the contrast depends strongly on the atomic number of the elements; [57] therefore, elemental U should appear much brighter than Fe and O. Figure 2a depicts several particles where uranium is clearly visible as white spots due to its higher contrast. Figure 2b displays an 8 nm particle orientated along the [100] projection, with the FFT (inset, top left) that can be indexed assuming *Fd*-3*m* symmetry. The structure is also represented (inset, bottom right), with Fe cations brown and O anions red
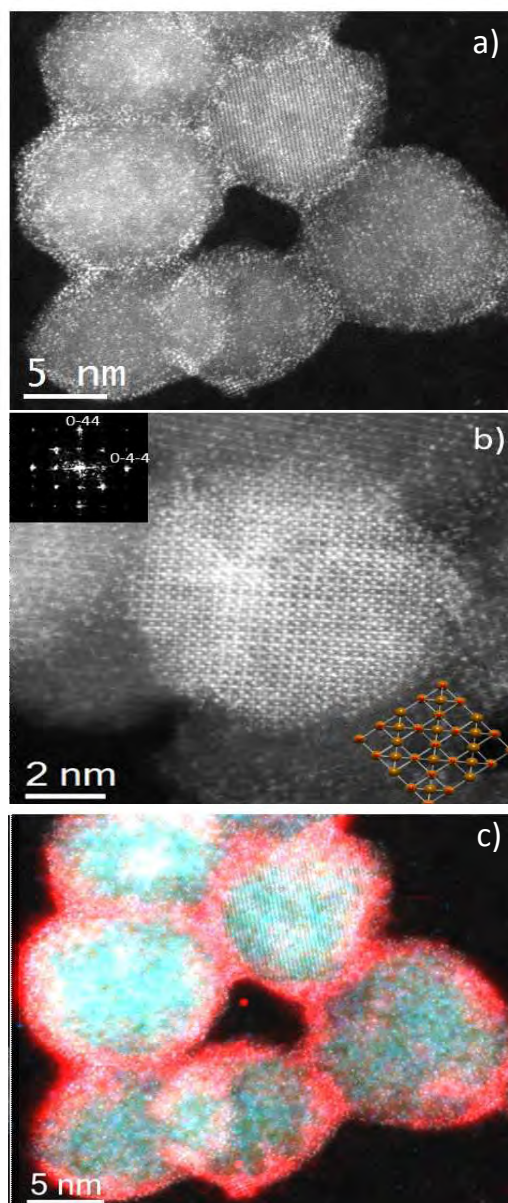
Figure 2. a) and b) High-resolution C_s-corrected STEM-HAADF images. c) STEM image with superimposed U (red), Fe (green) and O (blue).

ARTICLE

Environmenal Science: Nano

Electron Energy Loss Spectroscopy (EELS) was performed to corroborate the nanoparticle composition. The compositional map of the extracted signals is presented in Figure 2c superimposed on the experimental image. This image confirms that the nanoparticles consist of Fe and O coated with U ions. The extracted spectrum signal is shown in Figure S5 as well as each individual map.

The low-temperature magnetization curves of the SβCD-APTES@Fe$_2$O$_3$ nanocomposite before and after an adsorption test are shown in Figure S6. The samples are saturated at maximum external field. The saturation magnetizations of γ-Fe$_2$O$_3$ and SβCD-APTES@Fe$_2$O$_3$ NPs are 84.6 and 70.2 emu g^{-1}, respectively, corresponding to a net drop of 17% for the latter. This is a consequence of the non-magnetic layer of silica and organic compounds (SβCD-APTES) grafted at the surface of γ-Fe$_2$O$_3$.

The magnetization of the SβCD-APTES@Fe$_2$O$_3$ nanocomposite falls by a further 9% upon complexation but is still high enough to allow its magnetic harvesting by applying an external magnet.

2.2 Adsorptive features

2.2.1 Thermodynamics. The thermodynamic parameters of the interaction between SβCD with U(VI) are evaluated by ITC. Heat is either generated or absorbed when substances bind.[7] Figure 3A shows the raw ITC data for the titration of SβCD in water by uranyl acetate, where the decrease in the heat peak after each U(VI) injection implies the exothermic binding of U(VI) to SβCD. The quantity of heat decreases with increase in the molar ratio of U(VI) to SβCD and reaches a near-zero value when thermodynamic equilibrium is attained.

The ITC data fit the one-site model well (Figure 3A, Table 1), giving an equilibrium constant K$_a$ = 2.98 x 10^5 M^{-1} with a U(VI)/SβCD stoichiometry of 1.5, indicating that three U(VI) ions coordinate with two SβCD molecules in the presence of water. The three U(VI) are located in distorted octahedral complexes, two of them with the OH groups inside the cyclodextrins and the third with the succinyl groups between the cyclodextrins (Scheme 1). The complexation of uranium with SβCD is strongly exothermic (ΔH = -61.9 kJ mol^{-1}) with a calculated ΔG of -31.3 kJ mol^{-1} at 25 °C. More importantly, ITC measurements showed that the grafting of SβCD onto APTES@Fe$_2$O$_3$ leads to an almost 10-fold increase in the affinity for uranium due to the better organization of SβCD on the nanoparticles (Scheme 1, Figure 3B, Table 1). In both cases, with and without APTES@Fe$_2$O$_3$, the negative value of ΔG indicates that uranium adsorption onto SβCD is a spontaneous process.
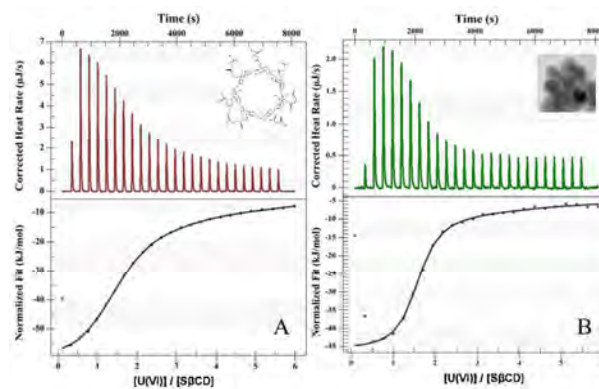

Figure 3. ITC measurement of exothermic binding of: (A) SβCD and U(VI) acetate (B) SβCD-APTES@Fe$_2$O$_3$ and U(VI) acetate at pH 6 and 25 °C. Titration plot derived from the integrated heats of binding corrected for the heat of dilution.

	SβCD	SβCD-APTES@Fe$_2$O$_3$
K$_a$ (M^{-1})	2.98.10^5	2.39.10^6
n	1.5	1.5
ΔH (kJ mol^{-1})	-61.9	-45.8
ΔS (J mol^{-1} K^{-1})	-103	-31.5
ΔG (kJ mol^{-1})	-31.3	-36.4

Table 1. Thermodynamic binding parameters obtained by fitting the ITC experiments.

2.2.2 Effect of initial pH on the extraction of uranium. The pH plays an important role on the overall sorption process and, more precisely, on the sorption capacity, as it can affect the surface charge of the sorbent, the degree of ionization of the material, and the dissociation of functional groups, such as carboxylate, hydroxyl and amino, present at the surface of the sorbent. It can also perturb the aqueous chemistry of uranium.[8, 58] The influence of the pH of the initial solution was investigated in the pH 2–8 range, adjusted by using either 0.2 M HNO$_3$ or 0.2 M NaOH solutions. Figure 4A clearly shows that the sorption capacity is highly pH-dependent, increasing from 11 mg U g^{-1} to 228 mg U g^{-1} as the pH rises from 2 to 6 and then sharply decreasing to 71.4 mg U g^{-1} at pH 8. The observed trends are related to both the distribution of U(VI) species and the surface charges on SβCD-APTES@Fe$_2$O$_3$. The proto-dissociation of functional groups can promote or suppress metal ion sorption. Indeed, when the pH increases the surface of SβCD-APTES@Fe$_2$O$_3$ gradually becomes more negatively charged (zeta potential at pH 6 = -20 mV) because of the deprotonation of the carboxylate groups (Figure 4B). At pH 2–6 the most predominant uranium species are UO$_2^{2+}$, (UO$_2$)$_3$(OH)$_5^+$ and (UO$_2$)$_4$(OH)$_7^+$ whereas at pH > 6 uranium is present mainly as (UO$_2$)$_3$(OH)$_7^-$ and (UO$_2$)(OH)$_3^-$.[7, 12] This leads to repulsion between the uranyl species and the sorbent, which probably explains the sharp decrease in the sorption capacity above pH 6.
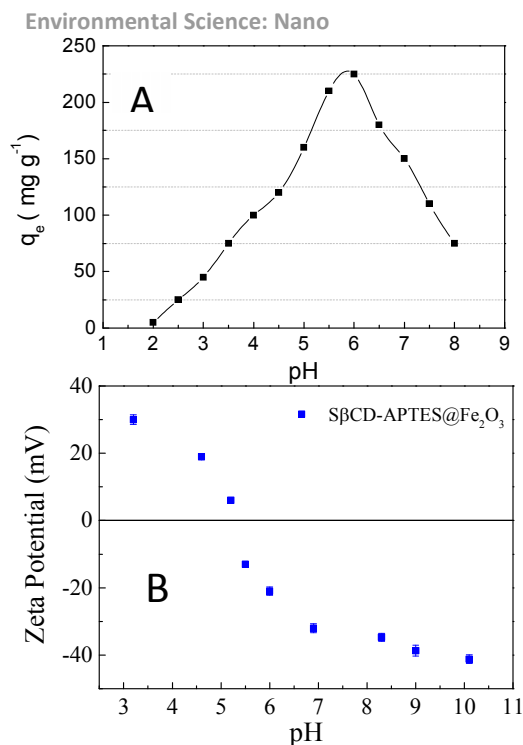
Figure 4. (A) Effect of pH on uranium adsorption by SβCD-APTES@Fe$_2$O$_3$ (180 min at 25 °C). (B) Zeta-potential of SβCD-APTES@Fe$_2$O$_3$

2.2.3 Kinetics of the adsorption of uranium. For the purpose of practical applications, the kinetics of sorption of U(VI) is investigated. Figure 5 shows the removal of U(VI) by SβCD-APTES@Fe$_2$O$_3$ NPs as a function of the contact time. The sorption of U(VI) onto SβCD-APTES@Fe$_2$O$_3$ increases rapidly in the first hour, and then attains a plateau after 3 hours (Figure 5). The experimental data are analyzed by pseudo-first-order, [59] pseudo-second-order, [60] and intra-particle diffusion[61] models.

The linear form of the pseudo-first-order rate equation is given as:

$$log(q_e - q_t) = logq_e - \frac{k_1}{2.303}t \qquad (1)$$

where q_e and q_t are the amounts of adsorbed UO_2^{2+} in mg g^{-1} at equilibrium and time t, respectively; k_1 the first-order adsorption rate constant in min^{-1}.

The linear form of the pseudo-second-order model is given by equation 2:

$$\frac{t}{q_t} = \frac{1}{k_2 q_e^2} + \frac{1}{q_e}t \qquad (2)$$

where k_2 the second-order adsorption rate constant in g mg^{-1} min^{-1}; q_e the adsorption capacity at equilibrium (mg g^{-1}).

The intra-particle diffusion model is expressed by equation 3:

$$q_t = k_p t^{1/2} + C \qquad (3)$$

where k_p is the intra-particle diffusion rate constant in mg g^{-1} min$^{-0.5}$; C the adsorption constant.

Table 2 shows the parameters of the different kinetic models for uranium adsorption. The correlation coefficients (R^2) for the best regression lines for the pseudo-first-order (equation 1), pseudo-second-order (equation 2) and intra-particle diffusion (equation 3) models are 0.9587, 0.9994 and 0.8789, respectively. The pseudo-second-order model (equation 2, Figure 5, Table 2) clearly best

describes the kinetics of the adsorption of uranyl on SβCD-APTES@Fe$_2$O$_3$.
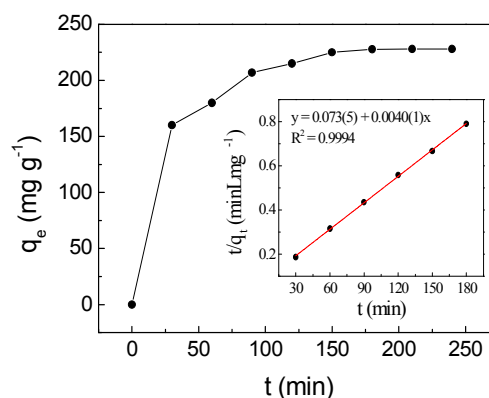
Figure 5. Effect of contact time on uranium adsorption by SβCD-APTES@Fe$_2$O$_3$; (inset) pseudo-second-order kinetic plot for adsorption of U(VI) (C$_0$ = 150 mg L^{-1}, pH 6, at 25 °C).

This suggests that chemisorption is the rate-controlling step, implying complex formation between adsorbent and adsorbate.[60] The carboxylate groups of the succinyl moieties and the hydroxyl groups inside the cyclodextrin cavity are responsible for metal complexation.

Kinetic model	Parameter	value
Pseudo-first-order	k_1 (min^{-1})	0.03
	$q_{e,cal}$	204.2
	R^2	0.9587
Pseudo-second-order	k_2 (g mg^{-1} min^{-1})	2.2 x10^{-4}
	q_e (mg g^{-1})	250
	R^2	0.9994
Intra-particle diffusion	k_p (mg g^{-1} min$^{-0.5}$)	16.6
	R^2	0.8789

Table 2: Pseudo-first-order, pseudo-second-order, and intra-particle diffusion kinetic models. Parameters for uranium adsorption.

2.2.4 Adsorption isotherms. The adsorption process was evaluated through different isotherms: Langmuir, Freundlich, Temkin, Elovich and Hasley (Figure 6, Table 3).

The experimental data were first evaluated using the Langmuir model, [61, 62] which is expressed by equation 4:

$$\frac{C_e}{q_e} = \frac{1}{q_{max}}C_e + \frac{1}{K_L q_{max}} \qquad (4)$$

where q_e is the sorption capacity at equilibrium; q_{max} the saturation sorption capacity; C_e (mg L^{-1}) the U(VI) concentration in solution at

ARTICLE

Environmenal Science: Nano

equilibrium; K_L (L mg^{-1}) the Langmuir constant directly related to the binding-site affinity.

This model assumes that: [63] (i) the solid surface presents a finite number of identical sites which are energetically homogeneous; (ii) there is no interaction between adsorbed species, meaning that the amount of adsorbate has no influence on the rate of adsorption, and (iii) the solid surface is saturated when a complete monolayer is formed. As shown in Figure 6a, the equilibrium data fit the Langmuir model well. q_{max} and K_L were obtained by plotting C_e/q_e versus C_e (equation 4, Table 3). SβCD-APTES@Fe$_2$O$_3$ exhibits a maximum sorption capacity (q_{max}) of 286 mg of U(VI) per g of sorbent at pH 6 in simulated contaminated water. SβCD-APTES@Fe$_2$O$_3$ appears to have a higher sorption capacity for U(VI) than other cyclodextrin derivatives (Table 4). The essential characteristic of the Langmuir isotherm can be expressed in terms of a dimensionless constant, commonly known as the separation factor (R_L) defined by Webber and Chakkravorti (equation 5): [64]

$$R_L = \frac{1}{1 + K_L C_0} \qquad (5)$$

where C_o is the initial adsorbate concentration (mg L^{-1}). The R_L value is related to strength of the adsorption. Indeed, $R_L > 1$, $R_L = 1$, $0 < R_L < 1$ and $R_L = 0$, imply weak, linear, strong or irreversible adsorptions, respectively.

where K_F is a constant related to the adsorption capacity (L g^{-1}), and 1/n is an empirical parameter related to the adsorption intensity which varies with the heterogeneity of the material.

	Langmuir		Freundlich		Temkin		Elovich		Halsey	
q_{max} (mg g^{-1})	286		K_F (L g^{-1})	53.7	a	39	K_E	0.63	K_H	3510
K_L (L mg^{-1})	0.18		1/n	0.5	b	60	q_m	120.5	n_H	2.04
R_L	0.04		n	2						
R^2	0.9932		0.9929		0.9829		0.9983		0.9899	

Table 3. Parameters of Langmuir, Freundlich, Temkin, Elovich, and Halsey isotherms for uranium adsorption.

The Freundlich parameters are obtained from the plot in Figure 6b, and are reported in Table 4. K_F can be used to explore the efficacy of the adsorption process.[65] The higher the capacity, the higher K_F, which is 53.7 in the present case, implying a strong interaction between sorbent and metal. Furthermore, the value of 1/n describes the adsorption intensity or the surface heterogeneity. A value of 0.5, between 0 and 1, indicates chemisorption.[66] According
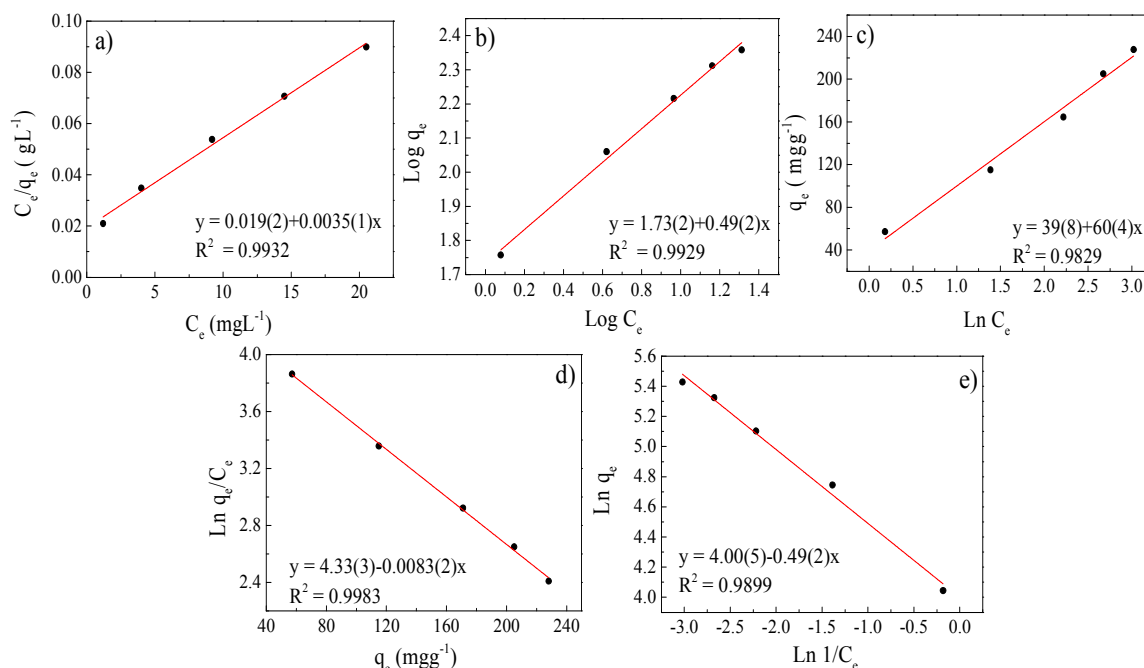

Figure 6. Uranium adsorption isotherms: (a) Langmuir; (b) Freundlich; (c) Temkin, (d) Elovich and (e) Halsey.

The Freundlich isotherm is one of the most widely used isotherms for the description of adsorption equilibria. This model assumes a heterogeneous adsorption surface and active sites, and the corresponding equation can be expressed in the linearized logarithmic form (equation 6):

$$log q_e = log K_F + \frac{1}{n} log C_e \qquad (6)$$

to our results (Table 4) the adsorption process involves complexation, which is in good agreement with the thermodynamic (ITC measurements) and kinetic investigations.

Sorbent	Capacity (mg g⁻¹) (reference)
Magnetite nanoparticles	5 ([70])
Multi-walled carbon nanotubes grafted with carboxymethyl cellulose	112 ([71])
Amine-functionalized magnetic-chitosan nanoparticles	178 ([8])
Quercetin-modified Fe_3O_4 NPs	12.3 ([72])
Polyamidoxime-functionalized NPs	247 ([73])
Di-amidoxime-functionalized NPs	120 ([74])
Fungus-Fe_3O_4 bio-nanocomposites	171 ([5])
Multi-walled carbon nanotubes grafted with chitosan	34.5 ([32])
β-Cyclodextrin/Al(OH)₃	63.3 ([75])
β-Cyclodextrin/montmorillonite/iron oxide	66.4 ([76])
Cyclodextrin-modified graphene oxide nanosheets	97 ([77])
β-Cyclodextrin/magnetic HNT/iron oxide composite	107.5 ([7])
SβCD-APTES@Fe_2O_3 NPs	286 (This work)

Table 4. Sorption capacity of U(VI) for various nanomaterials

The Temkin isotherm takes into account also the interactions between adsorbent and adsorbate. It is based on the assumption that the free energy of adsorption is a function of the surface coverage. The simplified form of this model,[67-69] developed considering only chemisorption, is expressed by the following linear relationship, equation 7:

$$q_e = a + b \, logC_e \qquad (7)$$

where a and b are the Temkin constants. A good regression line of q_e against $logC_e$ is obtained (Figure 6c) fitting this model quite well. a and b are determined from the intercept and slope of the regression line (Figure 6c, Table 3).

A very good least-squares regression line of $ln\frac{q_e}{C_e}$ against q_e (equation 8)[78] is obtained for the Elovich isotherm model (Figure 6d, Table 3).

$$ln\frac{q_e}{C_e} = -\frac{q_e}{q_m} + ln(K_E \cdot q_m) \qquad (8)$$

with K_E, the Elovich equilibrium constant (L mg⁻¹) and q_m, the Elovich maximum adsorption capacity.

Finally, the Halsey isotherm model is used to evaluate the multilayer adsorption system for metal ions at a relatively large distance from the surface,[61,62] according to equation 9:

$$ln(q_e) = \left[\left(\frac{1}{n_H}\right)ln(K_H)\right] - \left(\frac{1}{n_H}\right)ln\left(\frac{1}{C_e}\right) \qquad (9)$$

where K_H and n_H are the Halsey constants which can be obtained from the slope and intercept of the linear plot of $ln(q_e)$ versus $ln(C_e)$ (Figure 6e, Table 3).

Therefore, when all the techniques are taken together, we can conclude that the adsorption of uranyl ions on SβCD-APTES@Fe_2O_3 is mainly chemisorption. The q_e obtained for the sample of Figure

2c is 115 mg g⁻¹ which is equivalent to 800 atoms of U per nanoparticle. This Figure visualizes the U(VI) at the surface of SβCD-APTES@Fe_2O_3 and is consistent with the Hasley isotherm model for the adsorption of U(VI) in a multilayer.

2.2.5 Selectivity and reusability. In order to evaluate the selectivity of the nanocomposite, the effect of coexisting ions on U(VI) sorption is examined by using a solution containing 100 ppm of Cs^+, K^+, Mg^{2+}, Na^+, Al^{3+}, and UO_2^{2+}. In previous work, [79] we showed that SβCD has a good affinity for Cs^+ but not as much as for UO_2^{2+}. However, as shown in Figure 7A, the adsorption efficiency for uranium decreases by 36% due to the matrix effect of these cations, which exhibit the following affinity sequence: U(VI) > Cs^+ > Al^{3+} ≈ Mg^{2+} > K^+ ≈ Na^+ for the adsorbent at pH 6. This affinity sequence is corroborated by ITC (Figure 7B). The greater the heat released, the stronger the interaction between the molecules. This shows that SβCD-APTES@Fe_2O_3 has a much higher affinity for U(VI) than for the other ions. In order to reduce the matrix effect and to increase the extraction ratio, it would be necessary to optimize the quantity of adsorbent.
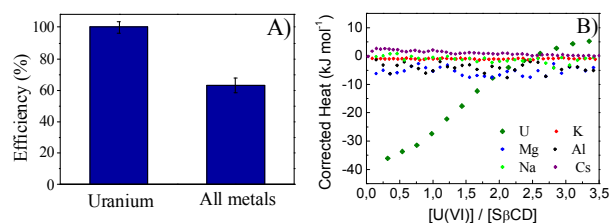

Figure 7. A) Selectivity of the SβCD-APTES@Fe_2O_3 nanocomposite for U(VI) in a solution of U(VI) acetate (100 %) and in a solution containing a mixture of U(VI) and five other metal cations (64%). B) Comparison of ITC measurements for binding of SβCD-APTES@Fe_2O_3 with U(VI) and other ions.

Tests showed that a small volume of 0.02 M HNO_3 efficiently desorbs U(VI) ions: 45 min of contact are sufficient to achieve the desorption equilibrium. Therefore, in a real case, the uranium desorbed by this process is concentrated before being sent to the company that manages the nuclear waste. Commercial extraction resins are plagued with issues such as their lack of reusability and the elution of the organic extractant/stationary phase. SβCD-APTES@Fe_2O_3 is much more robust. The sorption and desorption cycles are repeated ten times, to probe the regeneration ability of the system. From Figure 8, it is manifest that SβCD-APTES@Fe_2O_3 sorbents can be reused, indicative of the excellent stability of the organic ligands on the surface of γ-Fe_2O_3. After four adsorption/desorption cycles, there is no change in the efficacy of extraction/elution or morphology of the sorbent. After ten cycles, this decreases to 91% but no magnetic loss is detected. Thus, although SβCD is somewhat expensive, the SβCD-APTES@Fe_2O_3 nanocomposite is one of the most selective and robust materials for extraction of uranium from aqueous media by adsorption.
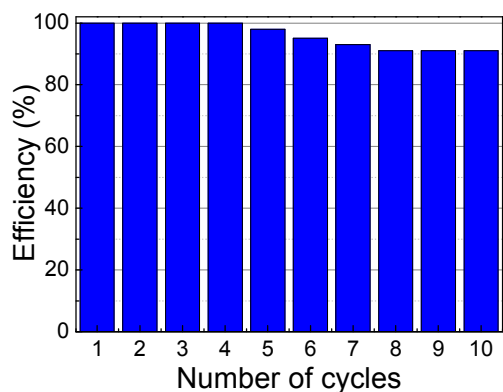
ARTICLE

Environmenal Science: Nano

Figure 8. Reusability tests on SβCD-APTES@Fe₂O₃ NP sorbent

3. Experimental section

3.1 Reagents and analysis

Succinyl-β-cyclodextrin (SβCD) was purchased from Sigma–Aldrich (France). All chemicals were of the purest grades, purchased from Merck, Sigma Aldrich, Fluka, Acros and VWR. A stock solution of U(VI) was prepared by dissolving $UO_2(C_2H_3O_2)_2.2H_2O$ (1.7818 g) in 1 L of doubly distilled water acidified with HNO_3 (5 mL, 2 M) to give a U(VI) solution (1000 mg L^{-1}). Working standards were prepared by diluting different volumes of the stock solution to obtain the desired concentration. The concentration of U(VI) in treated solutions was estimated by Inductively Coupled Plasma - Mass Spectrometry (ICP-MS).

3.2 Nanoparticle synthesis and functionalization

Maghemite (γ-Fe₂O₃) nanoparticles were synthesized in two steps. i) Magnetite (Fe₃O₄) particles were prepared by the polyol method using an appropriate amount of iron(II) acetate as metal precursor and triethylene glycol (TEG) as solvent. [80] The temperature of the mechanically stirred mixture was increased at a rate of 6 °C min^{-1} up to the boiling point (230 °C) and maintained at this temperature for 3 h. The mixture was then cooled to room temperature. A black dispersion of magnetite Fe₃O₄ was obtained. ii) Magnetite (black) was oxidized to maghemite (brown) by several washes with hot water and centrifugation (15 min at 22500 rpm). Besides oxidation, this procedure also eliminated the adsorbed TEG residues. The brown powder was dried at 50 °C for several hours. The γ-Fe₂O₃ NPs were then functionalized with (3-amino-propyl)triethoxysilane (APTES). [81, 82] The NPs (100 mg) were dispersed by ultrasonication in methanol (10 mL) which was followed by the addition of ethanol (250 mL). APTES (1 mL) was added slowly to the above mixture which was then ultrasonicated for 1 h. The mixture was boiled under argon for 2 h and then cooled to room temperature. The APTES-functionalized NPs were washed at least 4 times with ethanol, and the dispersion was collected by sedimentation on a laboratory magnet and dried overnight at 50 °C.

3.3 Grafting SβCD onto APTES@Fe₂O₃ functionalization

To a solution of SβCD (1 mL) in 2-(N-morpholino)ethane-sulfonic acid (MES, 100 mM, pH 6) were added N-hydroxysuccinimide (NHS, final concentration: 3.75 mM) and 1-ethyl-3-(3-dimethylaminopropyl)carbodiimide (EDC, final concentration: 1.5 mM). The solution was then stirred for 1 h at room temperature. NPs (5 mg) were dispersed in TRIS buffer (1 mL, 50 mM) at 7.4 ≤ pH ≤ 9 and vigorously shaken for 1 h. The two solutions were then mixed and the suspension stirred overnight at 4 °C. The suspension was washed several times with TRIS buffer at pH 7.4.

3.4 Nanoparticle characterization

Phase identification of the nanopowder was performed at room temperature by X-ray diffraction (XRD) on a PANALYTICAL X'PERT PRO with Co-Kα radiation (40 kV, 40 mA) (λ = 1.789 Å) and a X'celerator detector (2θ range from 10 to 120°). Crystallite size was calculated by means of the FullProf suite[83] based on the Rietveld method. The magnetic properties of raw NPs, as well as those of the nanocomposite before and after complexation, were evaluated from the first emanation curves measured at 10 K with a maximum magnetic field of 5 T on a vibration sample magnetometer (VSM; 9600-1 LDJ, USA). The size and shape of the maghemite nanoparticles were analyzed on a JEOL-100 CX Transmission Electron Microscope (TEM) operating at 100 kV. The samples were prepared at room temperature by slowly evaporating a drop of the NPs, dispersed in ethanol, on amorphous carbon-coated copper grids.

SβCD-APTES@Fe₂O₃ and uranium-loaded SβCD-APTES@Fe₂O₃ were analyzed by X-ray Electron Spectroscopy (ESCALAB 250, Thermo VG Scientific equipped with a monochromatic Al Kα X-ray source at 1486.6 eV) at a spot size of 650 μm. The samples were stuck on sample holders using conductive double-sided adhesive tape and pumped overnight in the fast entry lock at ≈5 × 10^{-10} mbar prior to transfer to the analysis chamber. An electron flood gun was used for charge compensation. The pass energy was set at 100 and 40 eV for the survey spectra and the narrow regions, respectively. Data acquisition and processing were achieved with the AVANTAGE software version 4.67. Spectral calibration was determined by setting the main C_{1s} component to 285 eV.

Fourier Transform Infrared (FTIR) spectra were recorded on a Bruker Equinox spectrometer in the range 400–4000 cm^{-1} using KBr pellets of dried samples of the pre- and post-functionalized particles.

Zeta-potentials were measured at different pH, using 10^{-2} M KNO_3 as background electrolyte, on a Zetasizer Nano S from Malvern Instruments.

Thermal analyses (TG/DTA) were performed in air on a Setaram TGA92 apparatus; samples were heated from room temperature up to 800 °C at a rate of 20 °C min^{-1}.

Spherical aberration (C_s)-corrected scanning transmission electron microscopy (STEM) was performed using a FEI Titan XFEG operated at 300 kV. The electron microscope was equipped with a CEOS corrector for the electron probe, allowing a spatial resolution of 0.8 Å. It was also fitted with a high-angle annular dark-field (HAADF) detector, an EDAX EDS detector and a Gatan Tridiem energy filter for spectroscopic analyses.

The uranyl ion concentrations before and after the sorption experiments were obtained by ICP-MS on an Agilent 7900 Q-ICP-MSICP-MS. An aliquot of each uranyl solution was diluted in a solution of HNO_3 (0.5 M) until the ppb concentration range was reached.

3.4 Kinetic measurements

Sorbents of SβCD-APTES@Fe$_2$O$_3$ (0.005 g) were put in contact with uranyl acetate (15 mL, initial metal concentration (C_0): 150 mg U L^{-1}) at pH 6 for different contact times: 0, 30, 60, 90, 120, 150 and 180 min. At the end of each period, magnetic separation was performed and the residual uranium concentration in the supernatant was measured by ICP-MS. The value of q_e for each sample was then determined by the mass balance equation (equation 10):

$$q_e = \frac{(C_0 - C_e)}{m} \cdot V \qquad (10)$$

where V is the volume of the solution (L), and m is the mass of the sorbent (g).

3.5 Thermodynamic measurements

Nano-ITC titrations were carried out at 25 °C in water by using a nano-isothermal titration calorimeter Nano-ITC (TA Instruments, USA) having an active cell volume of 940 μL and a 250 μL stirring syringe. Measurements were run in the overfilled mode. The power curve (heat flow as a function of the time) was integrated through Nano Analyze (TA Instruments, USA) to obtain the gross heat evolved/absorbed in the reaction. The equipment was checked by running an electrical calibration. Before each titration, all solutions were thoroughly degassed under vacuum with magnetic stirring. The solution in the sample cell was stirred at 300 rpm to ensure rapid mixing of the titrant upon injection. Titrations were performed by an automated sequence of 25 injections, each of 10 μL of uranyl solution (0.4 mM) into the sample cell containing the SβCD solution (0.02 mM), spaced at 300 s intervals to ensure complete equilibration. The ITC experiments with SβCD-APTES@Fe$_2$O$_3$ nanoparticles were performed under the same experimental conditions. In this case the amount of SβCD grafted onto the NP surface was estimated from the iron concentration obtained by ICP and also from the weight % in TGA. Three titrations were carried out for each measurement, and the results fitted with the independent-site model of the Nano Analyze software (TA Instruments). The ITC experiments with Al^{3+}, K$^+$, Mg^{2+} and Na$^+$ were carried out using solutions of SβCD (0.02 mM) and a metal concentration of 0.4 mM. The injection volume and the number of injections were 5 μL and 25, respectively.

3.6 Sorption and desorption experiments

Batch experiments were carried out by contact of SβCD-APTES@Fe$_2$O$_3$ sorbent (0.005 g) with uranyl acetate (15 mL, initial metal concentration (C_0): 0, 25, 50, 75, 100, 150 mg U L^{-1}) in a stoppered conical flask. The samples were vortexed (at 2000 rpm) for 3 h at 25±1 °C. After equilibration, magnetic separation (Figure S7) was performed and the residual uranium concentration in the supernatant (C_e, mg U L^{-1}) in the aqueous phase was determined, while the concentration of metal ions sorbed onto the SβCD-APTES@Fe$_2$O$_3$ (sorption capacity, q_e, mg U g^{-1}) was obtained from equation 10.

All these experiments were run in triplicate and the experimental variation was systematically less than 3%.

The recycling and reusability of the sorbents were ascertained by comparing the sorption capacity at the end of each successive step in a series of 10 sorption/desorption cycles. Sorbent (0.02 g) was stirred with uranyl solution (100 mL, C_0: 150 mg U L^{-1}) for 3 h at 25 °C in a conical flask. After magnetic separation the sorbent was recovered and the uranium concentration in the supernatant was determined by equation 10. The metal-loaded sorbent (after being washed with demineralized water) was mixed with HNO_3 (0.02 M) for 45 min at 25 °C. The metal concentration in the supernatant was used to derive the desorption yield for each step (equation 10).

3.7 Selectivity test

The selectivity test was performed by shaking SβCD-APTES@Fe$_2$O$_3$ (0.005 g) in an aqueous solution (15 mL) containing 20 mg L^{-1} of UO$_2$(OAc)$_2$, MgCl$_2$, KCl, NaCl, Cs(OAc) and AlCl$_3$ for 3 h at pH 6 and 25 °C. The metal ions were analyzed by ICP-MS.

Conclusions

APTES is used to modify and functionalize magnetic nanoparticles with succinyl-β-cyclodextrin, to give succinyl-β-cyclodextrin-APTES@Fe$_2$O$_3$, a nanocomposite material which has remarkable potential for the recovery of uranium from aqueous solution. It is highly selective for uranium(VI), is stable in acid solution and has a long service life. The maximum sorption capacity for uranyl ions is close to 286 mg g^{-1} at pH 6. Nano-ITC shows that the adsorption process is exothermic and spontaneous, and the uptake kinetics are described by the pseudo-second-order model. The adsorption of U(VI) on SβCD-APTES@Fe$_2$O$_3$ is fitted by the Langmuir, Freundlich, Temkin, Elovich, and Halsey isotherms. XPS and FTIR measurements indicate that the uranium is adsorbed by complexation. C_s-corrected STEM-HAADF provides a very impressive image of the uranium multilayer on the nanocomposite surface.

Conflicts of interest

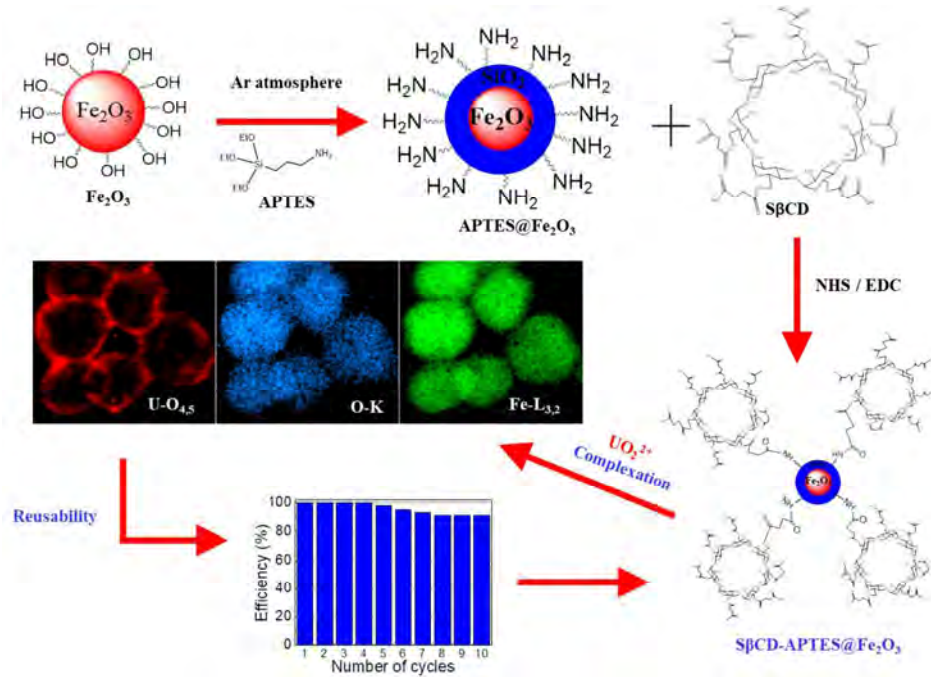There are no conflicts to declare.

ARTICLE

Environmenal Science: Nano

Notes and references

1. B. Cao, S. Fan, X. Tan, M. Li and Y. Hu, *Environ. Sci.: Nano*, 2017, **4**, 1670-1681.

2. M. R. Awual, S. Suzuki, T. Taguchi, H. Shiwaku, Y. Okamoto and T. Yaita, *Chem. Eng. J. (Amsterdam, Neth.)*, 2014, **242**, 127-135.

3. Y. Cai, C. Wu, Z. Liu , L. Zhang, L. Chen, J. Wang, X. Wang, S. Yang and S. Wang, *Environ. Sci.: Nano*, 2017, **4**, 1876-1886.

4. Z. Chen, Y. Liang, D. Jia, W. Chen, Z. Cui and X. Wang, *Environ. Sci.: Nano*, 2017, **4**, 1851-1858.

5. L. Li, M. Xu, M. P. Chubik, M. Chubik, A. A. Gromov, G. Wei and W. Han, *RSC Adv.,* 2015, **5**, 41611-41616.

6. P. Lestaevel, P. Houpert, C. Bussy, B. Dhieux, P. Gourmelon and F. Paquet, *Toxicology*, 2005, **212**, 219-226.

7. S. Yang, P. Zong, G. Sheng, Q. Wang and X. Wang, *Chem. Eng. J. (Amsterdam, Neth.)*, 2013, **214**, 376-385.

8. M. G. Mahfouz, A. A. Galhoum, N. A. Gomaa, S. S. Abdel-Rehem, A. A. Atia, T. Vincent and E. Guibal, *Chem. Eng. J. (Amsterdam, Neth.)*, 2015, **262** 198-209.

9. M. Tan, C. Huang, S. Ding, F. Li, Q. Li, L. Zhang, C. Liu and S. Li, *Sep. Purif. Technol.*, 2015, **146**, 192-198.

10. A. Rout, K. A. Venkatesan, T. G. Srinivasan and P. R. Vasudeva Rao, *J. Hazard. Mater.*, 2012, **221-222**, 62-67.

11. T. A. Lasheen, M. E. Ibrahim, H. B. Hassib and A. S. Helal, *Hydrometallurgy*, 2014, **14**, 175-182.

12. M. E. Ibrahim, T. A. Lasheen, H. B. Hassib and A. S. Helal, *J. Dispersion Sci. Technol.*, 2014, **35**, 599-606.

13. I. Doroshenko, J. Zurkova, Z. Moravec, P. Bezdicka and J. Pinkas, *Ultrason. Sonochem.*, 2015, **26**, 157-162.

14. G. I. Nkou Bouala, N. Clavier, R. Podor, J. Cambedouzou, A. Mesbah, H. P. Brau, J. Léchelle and N. Dacheux, *CrystEngComm*, 2014, **16**, 6944-6954.

15. R. Ruhela, N. Iyer, A. K. Singh, R. C. Hubli and J. K. Chakravartty, *Green Chem.*, 2015, **17**, 827-830.

16. A. C. Sather, O. B. Berryman and J. Rebek, *Chem. Sci.*, 2013, **4**, 3601-3605.

17. J. Qian, S. Zhang, Y. Zhou, P. Dong and D. Hua, *RSC Adv.*, 2015, **5**, 4153-4161.

18. C. Gunathilake, J. Górka, S. Dai and M. Jaroniec, *J. Mater. Chem. A*, 2015, **3**, 11650-11659.

19. S. D. Kolev, A. M. St John and R. W. Cattrall, *J. Membr. Sci.*, 2013, **425-426**, 169-175.

20. S. Panja, P. K. Mohapatra, S. C. Tripathi, P. M. Gandhi and P. Janardan, *J. Hazard. Mater.*, 2012, **237-238**, 339-346.

21. K. W. Kim, J. T. Hyun, K. Y. Lee, E. H. Lee, D. Y. Chung and J. K. Moon, *Eng. Chem. Res.*, 2012, **51**, 6275-6282.

22. M. L. Afonso, A. Gomes, A. Carvalho, L. C. Alves, F. Wastin and A. P. Gonçalves, *Electrochim. Acta*, 2009, **54**, 7318-7323.

23. M. Korenko, M. Straka, L. Szatmáry, M. Ambrová and J. Uhlíř, *J. Nucl. Mater.*, 2013, **440**, 332-337.

24. M. Khajeh, S. Laurent and K. Dastafkan, *Chem. Rev.*, 2013, **113**, 7728-7768.

25. Y. Wang, Z. Gu, J. Yang, J. Liao, Y. Yang, N. Liu and J. Tang, *Appl. Surf. Sci.*, 2014, **320**, 10-20.

26. S. Lee, W. Li, C. Kim, M. Cho, J. G. Catalano, B. J. Lafferty, P. Decuzzib and J. D. Fortner, *Environ. Sci.: Nano*, 2015, **2**, 500-508.

27. J. Florek, F. Chalifour, F. Bilodeau, D. Larivière and F. Kleitz, *Adv. Funct. Mater.*, 2014, **24**, 2668-2676.

28. N. Li, L. Zhang, Y. Chen, M. Fang, J. Zhang and H. Wang, *Adv. Funct. Mater.*, 2011, **22**, 835-841.

29. S. Choi and Y. Nho, *Radiat. Phys. Chem.*, 2000, **57**, 187-193.

30. A. J. Semiao, H. Rossiter and A. I. Schafer, *J. Membr. Sci.,* 2010, **348**, 174-180.

31. M. Manos and M. Kanatzidis, *J. Am. Chem. Soc.*, 2012, **134**, 16441–16446.

32. D. Shao, J. Hu and X. Wang, *Plasma Processes Polym.*, 2010, **7**, 977-985.

33. K. Hu, J. Sun, Z. Guo, P. Wang, Q. Chen, M. Ma and N. Gu, *Adv. Mater. (Weinheim, Ger.)*, 2015, **27**, 2507-2514.

34. R. Di Corato, A. Espinosa, L. Lartigue, M. Tharaud, S. Chat, T. Pellegrino, C. Menager, F. Gazeau and C. Wilhelm, *Biomaterials*, 2014, **35**, 6400-6411.

35. M. Mazario, A. Forget, H. Belkahla, J. S. Lomas, P. Decorse, A. Chevillot-Biraud, P. Verbeke, C. Wilhelm, S. Ammar, J. M. El Hage Chahine and M. Hémadi, *IEEE Trans. Magn.*, 2017, **53**, 1-6.

36. J. Hai, H. Piraux, E. Mazario, J. Volatron, N. T. Ha-Duong, P. Decorse, J. S. Lomas, P. Verbeke, S. Ammar, C. Wilhelm, J. M. El Hage Chahine and M. Hémadi, *J. Mater. Chem. B*, 2017, **5**, 3154-3162

37. Y. Liu, G. Zhang, Q. Guo, L. Ma, Q. Jia, L. Liu and J. Zhou, *Biomaterials*, 2017, **112**, 204-217.

38. Y. Wang and H. Gu, *Adv. Mater. (Weinheim, Ger.)*, 2014, **27**, 576-585.

39. S. Shylesh, V. Schünemann and W. R. Thiel, *Angew. Chem. Int. Ed.*, 2010, **49**, 3428-3459.

40. D. Yamaguchi, K. Furukawa, M. Takasuga and K. Watanabe, *Sci. Rep.*, 2014, **4**, 6053.

41. X. Zhang, J. Wang, R. Li, Q. Dai, R. Gao, Q. Liu and M. Zhang, *Ind. Eng. Chem. Res.*, 2013, **52**, 10152-10159.

42. M. Khoobi, M. Khalilvand-Sedagheh, A. Ramazani, Z. Asadgol, H. Forootanfarc and M. Faramarzia, *J. Chem. Technol. Biotechnol.*, 2014, **91**, 375-384.

43. A. Z. M. Badruddoza, A. S. H. Ta, P. Y. Tan, K. Hidajat and M. S. Uddin, *J. Hazard. Mater.*, 2011, **185**, 1177-1186.

44. J. Szejtli, *Chem. Rev.*, 1998, **98**, 1743-1754.

45. M. V. Rekharsky and Y. Inoue, *Chem. Rev.*, 1998, **98**, 1975-1918.

46. M. E. Skold, G. D. Thyne, J. W. Drexler and J. E. McCray, *J. Contam. Hydrol.*, 2009, **107**, 108-113.

47. S. S. Banerjee and D. H. Chen, *Nanotech.*, 2008, **19**, 265601-265607.

48. P. Castillo, M. Mata, M. Casula, J. Sanchez-Alcazar and A. Zaderenko, *Beilstein J. Nanotechnol.*, 2014, **5**, 1312-1319.

49. R. Chalasani and S. Vasudevan, *J. Mater. Chem.,* 2012, **22**, 14925-14931.

50. W. Wang, Z. H. Jin, L. Li, H. Zhang and S. Gao, *Chemosphere*, 2006, **65**, 1396-1404.

51. M. F. Hasan, A. M. Seyam and H. A. Hodali, *Polyhedron*, 1992, **11**, 1733-1736.

52. D. James, G. Venkateswaran and T. P. Rao, *Microporous Mesoporous Mater.*, 2009, **119**, 165-170.

53. A. M. Shallaby, M. M. Mostafa, K. M. Ibrahim and M. N. H. Moussa, *Spectrochim. Acta Part A,* 1984, **40**, 999-1002.

54. G. Tian, J. Geng, Y. Jin, C. Wang, S. Li, Z. Chen, H. Wang, Z. Zhao and S. Li, *J. Hazard. Mater.*, 2011, **190**.

55. A. Yacoutanour, A. K. T. Maki and M. M. Mostafa, *Spectrochim. Acta Part A*, 1988, **44**, 1291-1296.

56. A. J. Varma, S. V. Deshpande and J. F. Kennedy, *Carbohydr. Polym.*, 2004, **55**, 77-93.

57. A. Mayoral, T. Carey, P. A. Anderson and I. Diaz, *Microporous Mesoporous Mater.*, 2013, **166**, 117-122.

58. G. Crini, H. N. Peindy, F. Gimbert and C. Robert, *Sep. Purif. Technol.*, 2007, **53**, 97-110.

59. F. C. Wu, R. L. Tseng and R. S. Juang, *Water Res.*, 2001, **35**, 613-618.

60. J. Wang, R. Peng, J. Yang, Y. Liuc and X. Hu, *Carbohydr. Polym.*, 2011, **84**, 1169-1175.

61. J. Febrianto, A. N. Kosasih, J. Sunarso, Y. Ju, N. Indraswati and S. Ismadji, *J. Hazard. Mater.*, 2009, **162**, 616-645.

62. K. Y. Foo and B. H. Hameed, *Chem. Eng. J. (Amsterdam, Neth.)*, 2010, **156**, 2-10.

63. H. Parab, S. Joshi, N. Shenoy, R. Verma, A. Lali and M. Sudersanan, *Bioresour. Technol.*, 2005, **96**, 1241-1248.

64. T. W. Webber and R. K. Chakkravorti, *AIChE Journal,* 1974, **20**, 228-238.

65. A. D. Site, *J. Phys. Chem. Ref. Data*, 2001, **30**, 187.

66. F. Haghseresht and G. Q. Lu, *Energy Fuels*, 1998, **12**, 1100-1107.

67. K. Biswaw, S. K. Saha and U. C. Ghosh, *Ind. Eng. Chem. Res.*, 2007, **46**, 5346-5356.

68. C. Aharoni and M. Ungarish, *J. Chem. Soc. Faraday Trans.*, 1977, **73**, 456-464.

69. H. K. Boparai, M. Joseph and D. M. O'Carroll, *J. Hazard. Mater.*, 2011, **186**, 458-465.

70. D. Das, M. K. Sureshkumar, S. Koley, N. Mithal and C. G. S. Pillai, *J. Radioanal. Nucl. Chem.*, 2010, **285**, 447-454.

71. D. Shao, Z. Jiang, X. Wang, J. Li and Y. Meng, *J. Phys. Chem. B*, 2009, **113**, 860-864.

72. S. Sadeghi, H. Azhdari, H. Arabi and A. Z. Moghaddam, *J. Hazard. Mater.*, 2012, **215-216**, 208-216.

73. L. Huang, L. Zhang and D. Hua, *J. Radioanal. Nucl. Chem.,* 2015, **305**, 445-453.

74. M. Mazario, A. S. Helal, J. Stemper, A. Mayoral, P. Decorse, A. Chevillot-Biraud, S. Nowak, C. Perruchot, C. Lion, R. Losno, T. Le Gall, S. Ammar, J. M. El Hage Chahine and M. Hémadi, *AIP Adv.*, 2017, **7**, 056702.

75. C. Ding, W. Chengc, Z. Jina and Y. Suna, *Mol. Liq.*, 2015, **207**, 224-230.

76. J. Xiao, Y. Chen and J. Xu, *J. Ind. Eng. Chem. (Amsterdam, Neth.)*, 2014, **20**, 2830-2839.

77. W. Song, D. Shao and S. Lu, *Sci. China: Chem.*, 2014, **57**, 1291-1299.

78. S. Y. Elovich and O. G. Larinov, *Izv. Akad. Nauk SSSR, Otd. Khim. Nauk.*, 1962, **2**, 209-216.

79. A. S. Helal, P. Decorse, C. Perruchot, S. Novak, C. Lion, S. Ammar, J. M. El Hage Chahine and M. Hémadi, *AIP Adv.*, 2016, **6**, 056601

80. H. Basti, L. Ben Tahar, L. S. Smiri, F. Herbst, M. J. Vaulay, F. Chau, S. Ammar and S. Benderbous, *J. Colloid Interface Sci.*, 2010, **341**, 248-254.

81. D. Caruntu, B. L. Cushing, G. Caruntu and C. J. O'Connor, *Chem. Mater.*, 2005, **17**, 3398-3402.

82. H. Piraux, J. Hai, P. Verbeke, N. Serradji, S. Ammar, R. Losno, N. T. Ha-Duong, M. Hémadi and J. M. El Hage Chahine, *Biochim. Biophys. Acta*, 2013, **1830**, 4254-4264.

83. T. Roisnel and J. Rodriguez-Carvajal, *Mater. Sci. Forum*, 2000, **378-381**, 118-123.
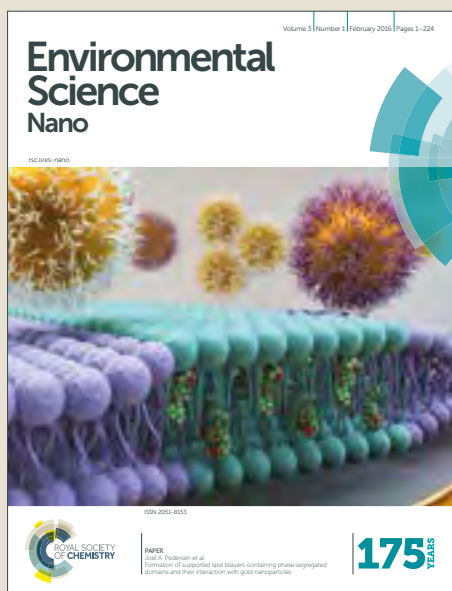
The production of low-carbon energy has considerable global influence on social, economic, and environmental development. Nuclear energy offers a very high energy density with extremely low greenhouse gas emissions with unparalleled advantages as compared to other energies. Uranium is mainly used as fuel in nuclear power-plants for electricity production in many countries, such as France, the United Kingdom, the United States, etc. To a lesser extent, uranium is also used in reactors for the propulsion of naval vessels, for basic and applied research, and for production of radioisotopes for multiple applications such as the treatment of cancer and medical imaging. Therefore, the release of hazardous radionuclides (e.g. ^{235}U, ^{238}U, ^{235}Np, ^{239}Pu, ^{247}Cm, ^{137}Cs, etc.) into the environment and aquatic system by various nuclear processes, such as mining operations, refining of nuclear fuel, aboveground/underground nuclear tests and during nuclear disasters (e.g. Three Mile Island in Pennsylvania in 1979, Chernobyl in 1986, and Fukushima Daiichi in 2011) represents a serious environmental problem and endangers human health. Hence, highly efficient concentration of uranium as well as its removal from aqueous solutions is of extreme importance for the optimal utilization of uranium resources, environmental protection and environmental repair. In France, the Socialist-Green political project involves stopping one third of the nuclear park. The shutdown, decommissioning and dismantling of nuclear power plants will inevitably lead to an increase in the amount of nuclear waste and in radioactive exposure of the workers on site. Therefore, a safe handling and disposal of nuclear waste is needed to avoid contamination. It is, thus, essential to find a cost-effective innovative system that can remove radioactive ions from nuclear waste-water and the contaminated surfaces of nuclear power plants. In this paper we propose an easy-to-implement nanocomposite device: ***succinyl-β-cyclodextrin-APTES@maghemite nanoparticles***, for sorting and concentrating radioactive waste, in this case U(VI) into a small volume.